Liquid State and Zombie Dye Sensitized Solar Cells with Copper Bipyridine Complexes Functionalized with Alkoxy Groups

Yasemin Saygili,[$] Marko Stojanovic,[$] Hui-Seon Kim, Joel Teuscher, Rosario Scopelliti, Marina Freitag, Shaik M. Zakeeruddin, Jacques-E. Moser, Michael Grätzel, and Anders Hagfeldt*

Read Online

ACCESS | Metrics & More | Article Recommendations | Supporting Information

ABSTRACT: Copper redox mediators can be employed in dye sensitized solar cells (DSCs) both as liquid electrolytes or as solid state hole transport materials (HTMs). The solid state devices that employ copper complex HTMs can be simply obtained by solvent evaporation in liquid state devices. During this evolution, the copper complex molecules present in the electrolyte solvent slowly aggregate in the pores of the TiO_2 film and also close the gap between the TiO_2 film and counter electrode. However, the crystallization of the HTM that infiltrated in the mesoscopic TiO_2 pores can lead to low photovoltaic performance. In order to prevent this problem, we designed two copper redox mediators $[Cu(beto)_2]^{1+}$ (beto = 4,4′-diethoxy-6,6′-dimethyl-2,2′-bipyridine) and $[Cu(beto_{2Ox})_2]^{1+}$ (beto$_{2Ox}$ = 4,4′-bis(2-methoxyethoxy)-6,6′-dimethyl-2,2′-bipyridine) with extended side chains. First, we studied these complexes in liquid state devices in reference to the $[Cu(tmby)_2]^{2+/1+}$ complex (tmby = 4,4′,6,6′- tetramethyl-2,2′-bipyridine). The solar-to- electrical power conversion efficiencies for liquid state devices were over 10% for all of the complexes by using the organic Y123 dye under 1000 Wm^{-2} AM1.5G illumination. However, solid state devices showed significantly diminished charge transport properties and short circuit current density values even though the crystallization was reduced.
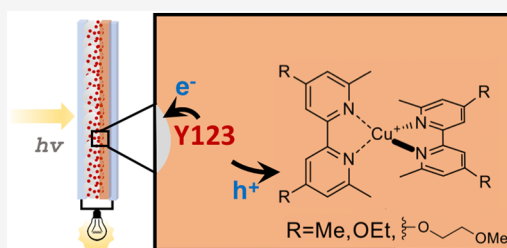
INTRODUCTION

Dye-Sensitized Solar Cells (DSCs) show promising potential as third generation photovoltaic (PV) technologies.[1,2] They offer energetically friendly fabrication processes in comparison to the silicon PV technology[3,4] and also satisfy aesthetic concerns. The employment of colored semitransparent glass and/or flexible substrates allows the easy integration of DSCs in buildings and electronic devices.[5,6] Recently, Cao et al. reported astonishing results for indoor light applications of DSCs with power conversion efficiency (PCE) values exceeding 32%.[7] The outstanding PCE values under ambient lightning makes DSC technology a favorable candidate to power low capacity portable electronic devices.[8]

The first DSC employing a ruthenium dye adsorbed on a mesoporous TiO_2 electrode and iodide/triiodide electrolyte was reported in 1991, with 7% PCE value under standard AM1.5G illumination.[9] Since then, many efforts have been made for developing new dyes,[10−14] electrolytes for liquid state devices,[15−18] and hole transport materials[19] (HTMs) for solid-state DSCs (ssDSCs) in order to advance the technology and increase the photovoltaic performance. With regard to electrolyte development, the replacement of the iodide/triiodide redox couple with organometallic redox shuttles has resulted in significant ameliorations. With organometallic redox shuttles, i.e., cobalt and copper complexes, dye regeneration is satisfied with a simple one electron transfer process following Marcus Theory,[20,21] whereas iodide/

triiodide follows a more complicated dye regeneration process. In addition, with metal complexes, the driving force for dye regeneration can be reduced significantly, hence an impressive improvement of the open circuit voltage (V_{OC})[22,23] while keeping a sufficient photocurrent[21,24,25] is feasible. These metal complex redox mediators showed their compatibility with a wide library of D-π−A/D-A-π−A[26−29] organic dyes. For ssDSCs, HTMs exist in a huge variety of inorganic and organic compounds.[19] Some of the common HTMs (and corresponding PCE values reported) for ssDSCs can be exemplified as CuSCN (2%),[30] CuI (4.5%),[31] poly(3,4-ethylenedioxythiophene) (PEDOT) (7.1%),[32] 2,2′,7,7′-tetrakis-(N,N-di-p-methoxyphenylamine)-9,9′-spirobifluorene (spiro-MeOTAD) (7.7%),[33] and Cs_2SnI_6 (7.8%).[34]

Surprisingly, in 2015, Freitag et al. reported the so-called "zombie cells"[35] by employing a $[Cu(dmp)_2]^{2+/1+}$ (dmp = bis(2,9-dimethyl-1,10-phenanthroline) redox mediator in DSCs. These ssDSCs were obtained simply by evaporating the volatile solvent from the liquid state DSC devices employing the $[Cu(dmp)_2]^{2+/+}$ electrolyte. With the slow evaporation of
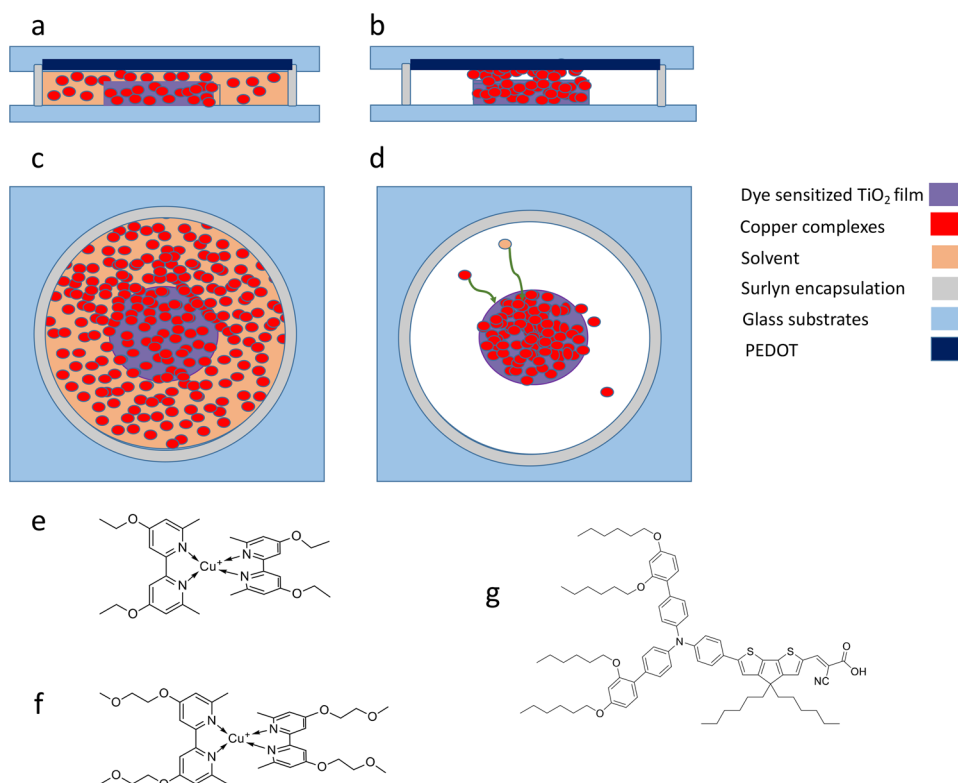
Figure 1. Schematic representations of liquid state DSC (a) side (c) top views and zombie device (b) side (d) top views, and molecular structures of (e) $[Cu(beto)_2]^{2+/1+}$, (f) $[Cu(beto_{2Ox})_2]^{2+/1+}$, (g) Y123 dye.

the solvent molecules, the copper species aggregated throughout the pores of TiO₂ and the TiO₂-counter electrode gap. These aggregated copper redox mediators function as a HTM (Figure 1a−d). Similarly, Kashif et al. reported solution-processable HTMs with cobalt polypyridyl complexes.[36] Later on, impressive PCEs of over 11% were reported for solid-state DSCs by employing $[Cu(tmby)_2]^{2+/1+}$ (tmby = 4,4′,6,6′-tetramethyl-2,2′-bipyridine) as a HTM.[37,38] An argument for the higher efficiencies with the Cu-complexes compared to those of other solid HTMs is that conventional ssDSCs, such as spiro-MeOTAD, suffer from the problems of inadequate pore filling.[39] The spin-coated HTMs result in low pore filling through the mesoscopic semiconductor. For example, for a 2.5 μm thick TiO₂ film, only 60−65% of the pores can be filled[39] via spin-coating. With this recent progress on the fabrication of solid-state DSCs with copper redox mediators,[35,37,38] thicker TiO₂ films can be employed and accordingly, better light harvesting is possible.

Crystallization[40] of the HTM is also reported to be detrimental to the performance of ssDSCs. The solid-state copper HTM can also exhibit morphological variations affecting the reproducibility and performance of the devices. Kovalevsky et al.[41] emphasized the importance of packing forces in crystalline environment for solid state $[Cu(dmp)_2]^{1+}$. Depending on the type of counterion, stacking interactions of the counterions and stacking modes of the ligands can show diversity, and $[Cu(dmp)_2]^{1+}$ can exhibit polymorphic modifications and/or cocrystallization with solvent molecules. According to the pioneering work of Freitag et al.,[35] copper HTMs reveal a partially crystalline structure and a significant part of the HTM is in an amorphous state with the $[Cu(dmp)_2]^{2+/1+}$ complex in ssDSCs. For $[Cu(tmby)_2]^{2+/1+}$, Cao et al.[37] reported that in some devices, the crystalline phase

was observed and that holes can be trapped at crystal grain boundaries. Crystallization of the HTM inside the porous structure and at the interfaces hinders the hole transport. Therefore, the short circuit current density (J_{SC}) values are influenced negatively especially with increasing light intensities. Thus, it is reported that an amorphous phase is preferred for better performances of the cell.

The morphology of HTM can be tuned by modifying the structure of the ligands of the copper complexes. Especially, introduction of aliphatic side chains on the ligand and introduction of an asymmetric ligand in the complex can help to reduce lattice packing and hence the crystallinity. Accordingly, in this study, we designed two new copper complexes by keeping the 6,6′-dimethyl-2,2′-bipyridine scaffold, which proved to be efficient at stabilizing Cu(I),[42,43] and by functionalizing the 4,4′ position with various side chains. With the introduction of $[Cu(beto)_2]^{1+}$ (beto = 4,4′-diethoxy-6.6′-dimethyl-2,2′-bipyridine) and $[Cu(beto_{2Ox})_2]^{1+}$ (beto₂Ox = 4,4′-bis(2-methoxyethoxy)-6,6′-dimethyl-2,2′-bipyridine) complexes, we aimed to hinder the crystallization at the interfaces of zombie devices through implementation of two different type of side chains at the 4,4′ positions. In regards to the aforementioned elements, we report the synthesis, characterization, as well as photovoltaic performances of new redox active copper complexes for both liquid and zombie DSCs. The chemical structures of the $[Cu(beto)_2]^{1+}$ and $[Cu(beto_{2Ox})_2]^{1+}$ are given in Figure 1e,f, respectively. In liquid state devices, DSCs employing the new copper redox mediators reached PCE values higher than 10% under full sunlight illumination (AM 1.5G) by showing similar characteristics to the reference complex $[Cu(tmby)_2]^{2+/1+}$ with the Y123 dye (Figure 1g). The X-ray diffraction (XRD) measurements on the solid-state DSCs showed that the introduction of the

aliphatic side chains (ethoxy and methoxyethoxy) to the ligands helped to reduce HTM crystallinity. However, the solidified versions of the new complexes resulted in very low PCE values. As observed by electrochemical impedance spectroscopy (EIS) and conductivity measurements, the charge transport ability of the HTMs decreased significantly. Diminished charge transport properties bring about the problems of reduced J_{SC}, V_{OC} values, and hysteresis.

■ EXPERIMENTAL SECTION

Synthesis of Ligands. The synthesis of the ligands was performed by reacting the commercially available 4,4′-dibromo-6,6′-dimethyl-2,2′-bipyridine with an excess of alcohol precursor previously treated by 3 equivalents of sodium hydride (NaH) at 90 °C overnight. The mixture was then poured over ice, and the ligands were extracted with dichloromethane (DCM) and subsequently dried to give the targeted structures: 4,4′-diethoxy-6.6′-dimethyl-2,2′-bipyridine (beto) and 4,4′-bis(2-methoxyethoxy)-6,6′-dimethyl-2,2′-bipyridine (beto$_{2Ox}$). The detailed synthetic procedure as well as characterization can be found in the Supporting Information.

Synthesis of Copper Complexes. The copper complexes were produced as previously reported.[25,35,44] In order to produce Cu(I) species, one equivalent of CuI was mixed with four equivalents of ligand in ethanol, under an inert atmosphere at room temperature. After 2 h, four equivalents of LiTFSI was added to the solution and mixing was continued for an additional 2 h. The red/orange Cu(I) powder was collected by filtering the stirred solution and washed with water and diethyl ether. The Cu(II) complexes were obtained by the addition of NOBF$_4$ to the electrolyte (direct oxidization of Cu(I) species). The details of the synthetic procedures are provided in Supporting Information.

Electrochemical Characterization. For cyclic voltammetry measurements, a three electrode setup was used, with a Ag/AgCl/saturated LiCl (ethanol) as reference electrode and platinum counter and working electrodes. The supporting electrolyte was a solution of 0.1 M LiTFSI or 0.1 M tetra-*n*-butylammonium hexafluorophosphate in acetonitrile. The concentrations of the $[Cu(beto)_2]^{1+}$ and $[Cu(beto_{2Ox})_2]^{1+}$ were 5.2 and 1.6 mM, respectively, and the scan rate was kept as 10 mV/s for each measurement. The measurements were carried out by Autolab Pgstat-30 potentiostat. The formal potential of the in situ Fc/Fc$^+$ couple was between 0.459 and 0.501 V vs our Ag/AgCl reference electrodes (Fc$^+$/Fc versus SHE (Standard Hydrogen Electrode) value is taken as +0.624 V).[45]

UV/vis absorption data for the copper complexes were gathered by a Hewlett-Packard 8453 diode array spectrometer. The extinction coefficients were calculated using the Lambert–Beer Law.

Single Crystal X-ray Diffraction. Single clear pale orange plate-shaped crystals of Cu(beto)$_2$TFSI were obtained by recrystallization from slow evaporation of an acetonitrile solution. A suitable crystal 0.67 × 0.38 × 0.21 mm^3 was selected and mounted on a suitable support on a SuperNova, Dual, Cu at home/near, AtlasS2 diffractometer. The crystal was kept at a steady T = 140.00(10) K during data collection. The structure was solved with the ShelXT (Sheldrick, 2015) structure solution program using the dual solution method and by using Olex2 (Dolomanov et al., 2009) as the graphical interface. The model was refined with version 2018/3 of ShelXL (Sheldrick, 2015) using Least Squares minimization.

X-ray Diffraction. X-ray diffraction (XRD) was measured by Empyrean (Panalytical) equipped with PIXel^{1D} (Panalytical) and a ceramic tube with Cu anode (λ = 1.54060 Å). Samples for XRD measurements were obtained by removing the PEDOT counter electrode of ss-DSCs or drop-casting of electrolytes on top of TiO$_2$ working electrode (FTO/TiO$_2$/Y123 substrates).

Device Fabrication. The working electrodes were prepared on cleaned FTO glasses (NSG-10, Nippon Sheet Glass). (The substrates were cleaned with a detergent (Deconex) in ultrasonic bath, and then treated with UV/O$_3$ (model no.256−220, Jelight Company, Inc.)) The TiO$_2$ underlayer was grown with a chemical bath deposition of TiCl$_4$ (53 mM). The mesoporous TiO$_2$ is obtained by screen printing 30 NRD (Dyesol) and scattering TiO$_2$ pastes (400 nm particle sized) as transparent (3 μm) and scattering layers (3 μm), respectively. The films were sintered with a ramped temperature profile, by keeping the substrates at 125, 250, 370, 450, and 500 °C for 5, 5, 5, 15, and 15 min, respectively, with a 5 min ramping duration between each temperature.

Following a sintering process at 500 °C for 30 min, the working electrodes were dipped into 0.1 mM of dye solutions (Dyenamo AB) in tert-butanol/acetonitrile (1:1 v/v) mixture for 16 h. In order to prevent aggregation, 0.4 mM chenodeoxycholic acid was used in the dye solutions.

The PEDOT counter electrodes were prepared by electrodeposition on FTO glasses (TEC 6, Pilkington).[46] Working and counter electrodes were assembled with melting a 25 μm Surlyn spacer (Dupont). For $[Cu(beto_{2Ox})_2]^{2+/1+}$, the electrolyte solutions contained 0.2 M Cu(I) and 0.05 M Cu(II) species, 0.1 M LiTFSI, and 0.6 M TBP in acetonitrile injected to the device through a predrilled hole by a vacuum pump. (Due to lower solubility of $[Cu(beto)_2]^{2+/1+}$ in acetonitrile, the beto electrolyte is more diluted and contains 0.07 M Cu(I) and 0.02 M Cu(II) species.) A detailed device fabrication method can be found in our previous publication.[25]

Transient Absorption Spectroscopy (TAS). The photoinduced kinetics was measured with an Ekspla NT-342 Q-switched Nd:YAG laser using 532 nm as excitation wavelength. The pulse width was 4−5 ns (fwhm), and the repetition rate was 20 Hz. The probe light source was a halogen lamp, and the probe wavelength at 715 nm was chosen using a monochromator. The film was positioned at approximately 45 degree angle with respect to the incoming laser pulse, for front illumination. The signal was detected using the photomultiplier tube R9110 from Hamamatsu and recorded using the oscilloscope DPO 7254 from Tektronix. The radiant output of the laser was attenuated using gray optical density filters to 46 μJ/cm^2, for the measurements of the samples containing redox mediators, and 1.27 μJ/cm^2 for the electrolytically inert samples. Low light intensity value was deliberately chosen in order to ensure that the data could be fitted to single exponential functions from which the lifetimes could be obtained. An acquisition was averaged over 3000 laser shots.

Electron Lifetime and Charge Extraction Measurements. DYENAMO Toolbox System was used to collect the electron lifetimes and charge extraction data. The Toolbox setup consists of a white LED light source (Seoul Semiconductors), a 16-bit resolution digital acquisition board (National Instruments), and a current amplifier (Thorlabs PDA200C). Prior to charge extraction, the DSCs were kept at open-circuit conditions and illuminated by the LED light. After 1 s, the light source was turned off and the device was switched

to short-circuit condition. Then the total extracted charge was integrated over time. In order to obtain a complete charge-potential curve, the measurement was repeated at different light intensities. In electron lifetime measurements, the light source was controlled by a modulated current superimposed on a bias current and the open-circuit voltage response was measured. The lifetimes were obtained by fitting parameters of open-circuit voltage response curves.

Solar Cell Characterization. The current−voltage ($I−V$) performances of the DSC devices were obtained by using a 450W xenon light source (Oriel, U.S.A). Schott K113 Tempax filter (Präzisions Glas & Optik GmbH) was used to reduce the spectral mismatches between AM 1.5G and the light source. A Keithley model 2400 digital source meter (Keithley, U.S.A) was used to apply an external potential bias to the devices and measure the resulting current. For $I−V$ measurements, we used a black mask with a 0.16 cm^2 aperture area.

Incident Photon to Current Conversion Efficiency (IPCE). IPCE data were acquired using a computer controlled setup consisting of a 300W xenon light source (ILC Technology, USA), a monochromator (JobinYvon Ltd., UK), and a Keithley 2700 multimeter.

Electrochemical Impedance Spectroscopy (EIS). Bio-Logic SP300 potentiostat was used to carry out impedance measurements. A sinusoidal potential perturbation was applied within a frequency range of 7 MHz-0.1 Hz. The bias potential was manipulated between 0 V and V_{OC}, with 50 mV increments. The impedance data was fitted with ZView software (Scribner Associates) according to the transmission line method.[47]

Conductivity. Two channel conductivity measurements were performed by using NanoSPR interdigitated electrodes. The electrolyte solutions were deposited on the electrodes by drop-casting. The current−potential data was gathered by a BioLogic SP30 potentiostat.

■ RESULTS AND DISCUSSION

Spectroscopic and Electrochemical Characterization. The UV/vis spectra of [Cu(beto)$_2$][TFSI] and [Cu(beto$_{2Ox}$)$_2$][TFSI] were recorded with a 0.5 mM acetonitrile solution of each complex. The absorbance measurements showed that both complexes have very similar spectral responses. Two local absorption maxima were found, lying around 334 and 440 nm for both [Cu(beto)$_2$][TFSI] and [Cu(beto$_{2Ox}$)$_2$][TFSI] (see Figure S1). The first peak, is attributed to a $\pi−\pi^*$ transition, originating from the 2,2′-bipyridine ligand conjugated network. Here, it is reasonable to assume that the wavelength at which the transition will occur will be influenced by the electronic substituents located on the 2,2′-bipyridine scaffold. In this case, both complexes showed a transition occurring at 334 nm. This would indicate that there is not a major influence on the electronic properties arising from the ether chain present in [Cu(beto$_{2Ox}$)$_2$][TFSI] . The second electronic transition occurs around 440 nm for both complexes and is attributed to a metal to ligand charge transfer transition (MLCT), which also seems to indicate similar photophysical properties between [Cu(beto)$_2$][TFSI] and [Cu(beto$_{2Ox}$)$_2$][TFSI]. The molar extinction coefficients were calculated and are reported in Table 1. They show similar values for both complexes for each discussed transition.

Cyclic voltammetry was used to probe the electrochemical activity of the newly synthesized complexes. As presented in Table 1 and Figure S2, the redox potentials of our complexes

Table 1. Absorption Data and Formal Redox Potentials of the Cu(1) Complexes

[Cu(L)$_2$][TFSI]	$\lambda_{\pi−\pi^*}$/ nm	$\varepsilon_{\pi−\pi^*}$/ M^{-1}×cm^{-1}	λ_{MLCT}/ nm	ε_{MLCT}/ M^1×cm^{-1}	E'^0/(V vs SHE)
L = beto	334	4.88×10^3	443	5.02×10^3	0.79
L = beto$_{2Ox}$	334	5.33×10^3	440	5.25×10^3	0.81

are around 0.8 V vs SHE. This shows similar electrochemical properties between the two complexes but also indicates that the ether chain present on beto$_{2Ox}$ does not alter its redox behavior. Our copper-complexes showed good electrochemical activity and reversibility upon several scans. In comparison to the unfunctionalized [Cu(dmby)$_2$]$^{2+/1+}$ (dmby = 6,6′-dimethyl-2,2′-bipyridine) complex, our ligands showed a downwardly shifted potential of approximately 0.2 V vs SHE. This effect is attributed to the π-electron donating oxygen atoms that were installed at the 4,4′ position of the ligands. They would increase the electron density of the copper center, via the ligand, hence increasing the reductive strength of the complex.

The state-of-the-art Cu[(tmby)$_2$]$^{2+/1+}$ complex offers a redox potential of 0.871 V vs SHE, while other 2,2′-bipyridine or phenanthroline based ligands produce a redox potential above 0.9 V vs SHE.[25] This limits the use of dyes with Highest Occupied Molecular Orbital (HOMO) levels that are more negative than 1 V vs SHE. (For example, Y123[25] (1.07 V vs SHE) and XY1[48] (0.99 V vs SHE) dyes showed compatibility with these redox mediators.) Considering the more negative formal redox potentials of [Cu(beto)$_2$]$^{1+}$ and [Cu(beto$_{2Ox}$)$_2$]$^{1+}$ complexes, we can presume that for these complexes, the choice of suitable dyes is higher.

Single Crystal X-ray Diffraction. Crystals suitable for X-ray diffraction were grown from slow evaporation at room temperature of an acetonitrile solution of [Cu(beto)$_2$][TFSI]. Unfortunately, this could not be achieved for [Cu(beto$_{2Ox}$)$_2$]-[TFSI] even after screening of different solvents as well as binary solvent mixture conditions. We speculate that this is due to the ethoxy−methoxy chains located at the 4,4′ position of [Cu(beto$_{2Ox}$)$_2$][TFSI] that would prevent an efficient molecular packing and hence crystallization of the molecule.

Figure 2 shows the ORTEP (Oak Ridge Thermal Ellipsoid Plot) representation of [Cu(beto)$_2$][TFSI] crystals. They

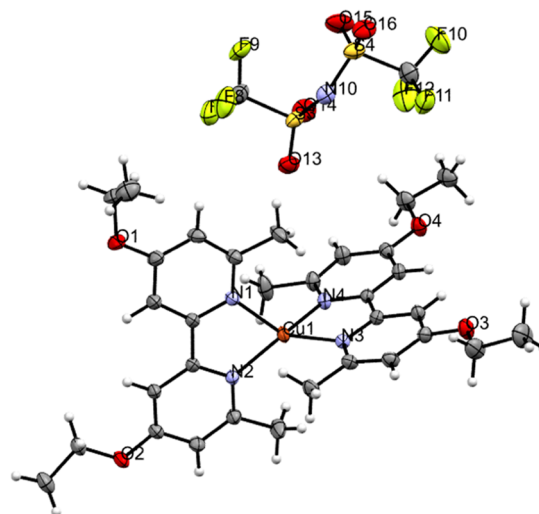**Figure 2.** OTREP representation of [Cu(beto)$_2$][TFSI].

essentially consist of isolated $[Cu(beto)_2]^{1+}$ with uncoordinated TFSI⁻ anions. As expected, the bipyridine ligand coordinates the central copper atom in a bidentate mode. The two methyl groups at the 6,6′ position prevent the ligands from twisting, which ultimately stabilizes the coordination complex in a strongly distorted tetrahedral geometry. The measured coordinating bond lengths were consistent and very close to 2 Å (see Table 2). There are three different sets of

Table 2. Crystallographic Data, Bond Lengths, and Angles of $[Cu(beto)_2][TFSI]$

Molecular formula	$C_{34}H_{40}CuF_6N_5O_8S_2$		
		Bond Length/(Å)	
MW/(g/mol)	888.37	Cu1−N1	2.061
Crystal system	Monoclinic	Cu1−N2	2.011
Space group	$P2_1/n$	Cu1−N3	2.040
a/(Å)	15.67850(11)	Cu1−N4	2.034
b/(Å)	23.18286(15)		
		Angle/(deg)	
c/(Å)	21.81083(15)	N1−Cu1−N2	80.89
α/(deg)	90	N2−Cu1−N3	132.26
β/(deg)	97.9481(7)	N3−Cu1−N4	80.94
γ/(deg)	90	N4−Cu1−N1	117.47
Cell Volume/(Å³)	7851.48(9)	N2−Cu1−N4	131.09
Z	8	N1−Cu1−N3	118.62

angles: the five membered ring chelate (N1−Cu1−N2 and N3−Cu1−N4) was close to 81° and two additional angles formed by the intercrossed ligand planes, N4−Cu1−N1 and N1−Cu1−N3, were around 118°, with N2−Cu1−N4 and N2−Cu1−N3 having values approaching 132°. Beside the five membered bidentate angles, the two other sets show strong fluctuation indicating an important distortion of the coordination geometry. The dihedral angle along the 2,2′ axis of the bipyridine shows very little torsion values of 3.12° and 0.84°, respectively. Reported Cu(I) complexes were found to have similar geometrical trends upon coordination of Cu(I) with

6,6′,4,4′-tetramethyl-2,2′-biypyridine or 6,6′-dimethyl-2,2′-biypridine ligands.[49,50]

X-ray Diffraction (XRD) Measurements. We analyzed the effect of the ligand structures of $[Cu(beto)_2]^{2+/1+}$ and $[Cu(beto_{2Ox})_2]^{2+/1+}$ complexes on the morphology of the HTM by X-ray diffraction (XRD) measurements on the FTO/TiO₂/Y123/HTM samples. The XRD data of the working electrodes of the opened DSC devices and the dried samples which were prepared by drop-casting are given in Figure 3a,b, respectively. As observed in Figure 3a, the $[Cu(beto_{2Ox})_2]^{2+/1+}$ (blue) and $[Cu(beto)_2]^{2+/1+}$ (red) do not exhibit any crystalline phases in zombie devices. As presumed, introduction of the aliphatic side chains (ethoxy and methoxyethoxy) reduced HTM crystallinity. The XRD pattern for the $[Cu(tmby)_2]^{2+/1+}$ complex shows the presence of 12 and 24 degree peaks (black line in Figure 3a), which are attributed to a partially crystalline phase. Drop-casting of the electrolyte solution provides a faster evaporation of the solvents, and the crystalline phase is expected to become more apparent. With the drop-casting method, for $[Cu(beto_{2Ox})_2]^{2+/1+}$, the amorphous phase is almost preserved by disregarding the low-lying peaks (red line in Figure 3b). In case of the $[Cu(beto)_2]^{2+/1+}$, the faster solvent evaporation results in a crystalline structure (blue line in Figure 3b), nonetheless, with less intense peaks in comparison to $[Cu(tmby)_2]^{2+/1+}$ (Figure S3). When the XRD data is considered, it can be stated that the slow evaporation of the electrolyte solvent is still necessary to inhibit the crystalline HTM and the detrimental effects.

Dye Regeneration and Charge Recombination Analysis with Liquid Electrolytes. In order to investigate the dye regeneration kinetics with the $[Cu(beto)_2]^{2+/1+}$ and $[Cu(beto_{2Ox})_2]^{2+/1+}$ liquid electrolytes, we performed nanosecond transient absorption spectroscopy (TAS) measurements. The recombination of injected electrons in the TiO₂ and oxidized dye molecules showed an absorbance decay signal with a 0.55 ms half-lifetime($\tau_{1/2}$) in the absence of redox species (only 0.1 M LiTFSI and 0.6 M TBP in acetonitrile) (see Figure 4). In the presence of our redox electrolyte, the absorbance signal
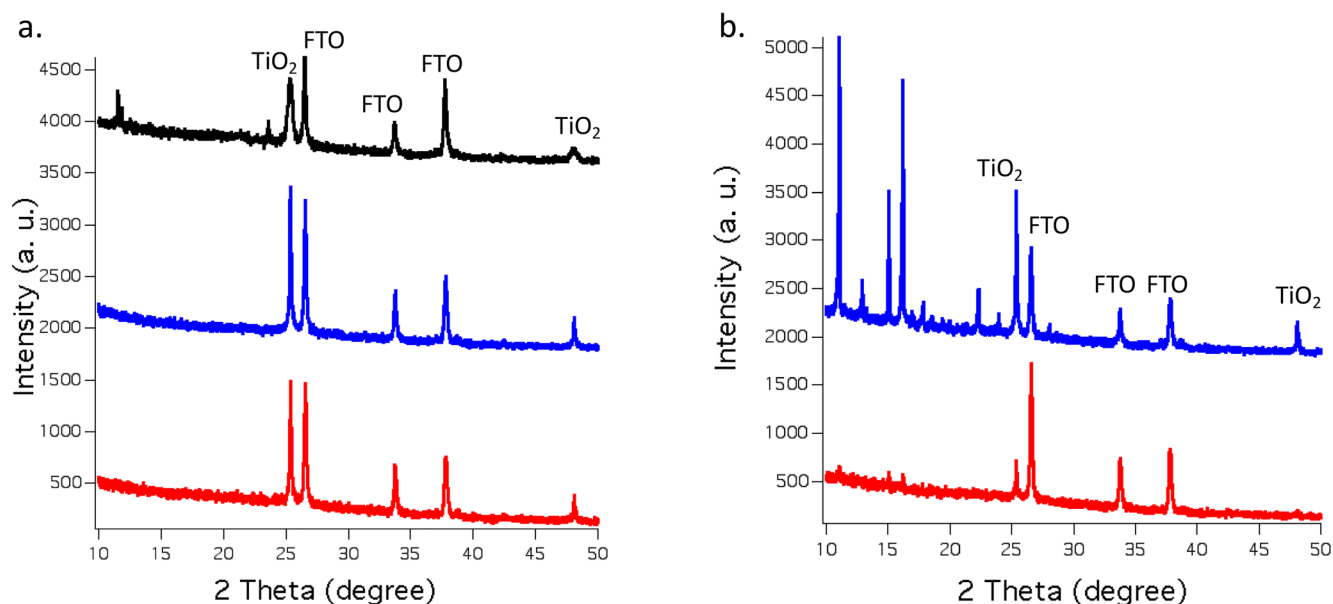

Figure 3. XRD data of (a) working electrode of opened ssDSC devices (FTO/TiO₂/Y123/HTM) ($[Cu(beto)_2]^{2+/1+}$ (blue), $[Cu(beto_{2Ox})_2]^{2+/1+}$ (red), and $[Cu(tmby)_2]^{2+/1+}$ (black)). (b) Dried electrolytes after drop-casting ($[Cu(beto)_2]^{2+/1+}$ (blue) and $[Cu(beto_{2Ox})_2]^{2+/1+}$ (red)).
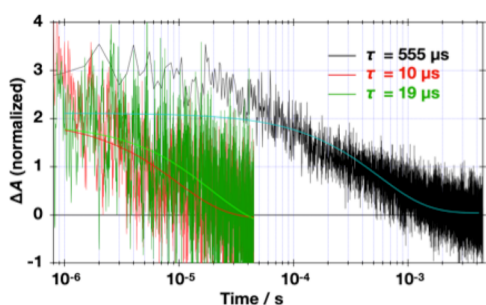
Figure 4. Transient absorption spectroscopy measurements of Y123-sensitized TiO$_2$ films with inert (black), $[Cu(beto_{2Ox})_2]^{2+/1+}$(red), $[Cu(beto)_2]^{2+/1+}$(green) electrolytes.

shows an accelerated decay, which indicates the regeneration of oxidized dye molecules by Cu(I) species. Under the same conditions, the regeneration halftimes of $[Cu(beto)_2]^{2+/1+}$ and $[Cu(beto_{2Ox})_2]^{2+/1+}$ are measured as 19 and 10 μs, respectively. Using eq 1, the regeneration efficiencies (Φ_{reg}) are calculated as 97% and 98% for the $[Cu(beto)_2]^{2+/1+}$ and $[Cu(beto_{2Ox})_2]^{2+/1+}$ complexes, respectively.

$$\Phi_{reg} = \frac{k_{reg}}{k_{reg} + k_{rec}} \quad (1)$$

In comparison to the previously reported $[Cu(tmby)_2]^{2+/1+}$complex,[25] $[Cu(beto)_2]^{2+/1+}$ and $[Cu(beto_{2Ox})_2]^{2+/1+}$ have bulkier ligand structures with the substitution of ethoxy and methoxyethoxy groups. The differences in regeneration efficiencies can be attributed to the differences in molecular structures and reorganization energies of these three copper complexes. As expected, the spatial separation of the donor and acceptor states with the extended 4,4′-bis(2-methoxyethoxy) groups of $[Cu(beto_{2Ox})_2]^{2+/1+}$ and 4,4′-diethoxy groups of $[Cu(beto)_2]^{2+/1+}$ will be higher and the electron transfer rates will be slower compared to $[Cu(tmby)_2]^{2+/1+}$ complex. Also, by considering the diffusional constraints of $[Cu(beto_{2Ox})_2]^{2+/1+}$ and $[Cu(beto)_2]^{2+/1+}$ in the mesoporous TiO$_2$ structure, smaller dye regeneration efficiency values are foreseen for the new complexes. Nevertheless, increased spatial separation and diffusion problems are compensated by the increased driving force for dye regeneration. Therefore, dye regeneration efficiencies stay closer to unity for $[Cu(beto)_2]^{2+/1+}$ and

$[Cu(beto_{2Ox})_2]^{2+/1+}$ complexes as in the case of $[Cu(tmby)_2]^{2+/1+}$.

We analyzed the recombination of the oxidized form of the redox species and the injected electrons in TiO$_2$ by electron lifetime and charge extraction measurements. The semilogarithmic plots of electron lifetime and charge extraction values with respect to the quasi-Fermi level of the electrons in TiO$_2$ are given in Figure 5a,b, respectively. At the same quasi-Fermi level of electrons in the TiO$_2$ electrode (-0.2 eV), the electron lifetimes in the presence of $[Cu(beto)_2]^{2+/1+}$, $[Cu(beto_{2Ox})_2]^{2+/1+}$, and $[Cu(tmby)_2]^{2+/1+}$complexes are 0.08, 0.03, and 0.008 s, respectively. By having a more positive redox potential and higher driving force for recombination, the $[Cu(tmby)_2]^{2+/1+}$ complex exhibits lower electron lifetime values due to higher recombination rates. These values show that the recombination reaction is driving force dependent similar to our previous studies.[51]

For the same extracted charge value, $[Cu(beto)_2]^{2+/1+}$ and $[Cu(beto_{2Ox})_2]^{2+/1+}$ exhibit a slightly negative shifted conduction bands in comparison to $[Cu(tmby)_2]^{2+/1+}$. This finding is attributed to a slightly more negative surface charge value for the $[Cu(beto)_2]^{2+/1+}$ and $[Cu(beto_{2Ox})_2]^{2+/1+}$ redox species. $[Cu(beto)_2]^{2+/1+}$ and $[Cu(beto_{2Ox})_2]^{2+/1+}$ showed the same extracted charge values through the whole potential range.

Photovoltaic Performances of the DSC Devices Employing the Y123 Dye. The photocurrent density–voltage (J–V) data of solar cells prepared by Y123 sensitized TiO$_2$ films that employed liquid state copper electrolytes are given in Figure 6a. The short-circuit current densities (J_{sc}), open circuit voltages (V_{oc}), fill factors (FF), and power conversion efficiencies (PCEs) of these devices are also given in Table 3. The PCE values are calculated by eq 2 where J_{sc} is the current density, V_{oc} is the open circuit voltage, FF is fill factor, and I_0 is the incident light intensity.

$$\eta = J_{sc} \times V_{oc} \times \frac{FF}{I_0} \quad (2)$$

For the liquid state devices employing $[Cu(tmby)_2]^{2+/1+}$, $[Cu(beto_{2Ox})_2]^{2+/1+}$, $[Cu(beto)_2]^{2+/1+}$, the PCE values above 10% were reached at AM 1.5 G illumination. The open circuit voltage values are above 1.0 V. The higher redox potential of the $[Cu(tmby)_2]^{2+/1+}$ complex would result in a higher photovoltage, but the longer electron lifetime for the new
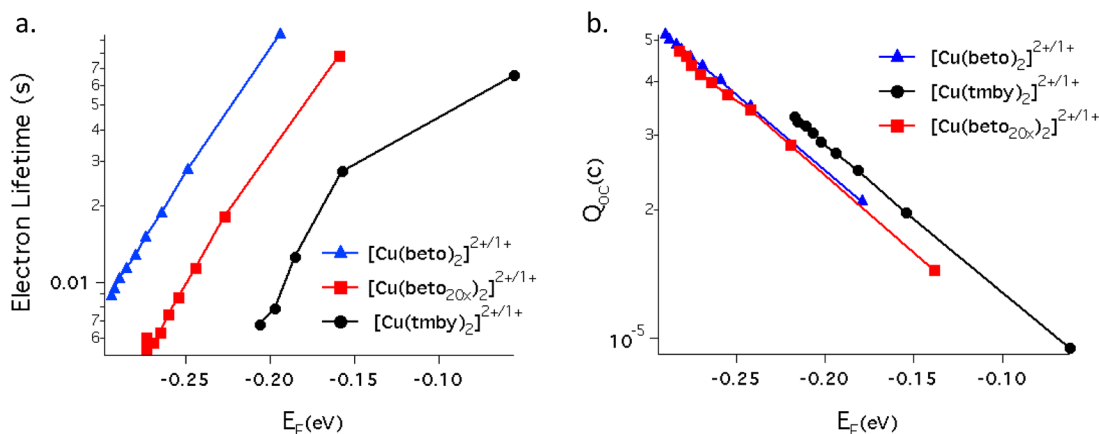

Figure 5. (a) Electron lifetime and (b) charge extraction values for the copper complexes. ($E_{F,TiO2} = E_{F,TiO2} - V_{oc}$).
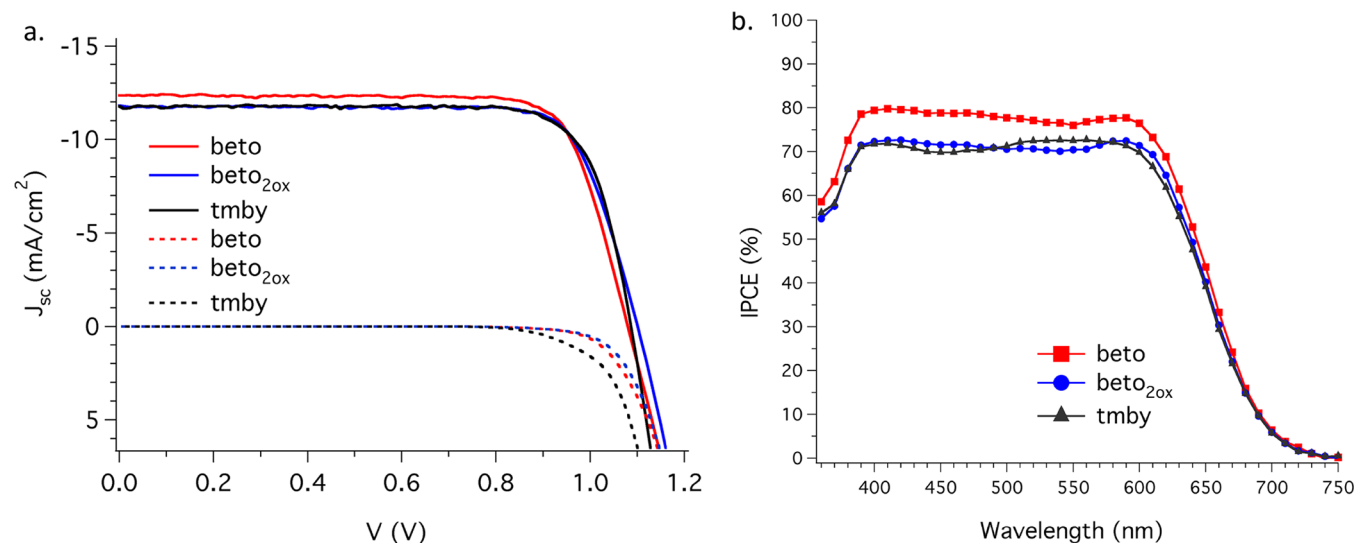
Figure 6. Photovoltaic characterization of the DSCs sensitized with Y123 dye employing $[Cu(tmby)_2]^{2+/1+}$, $[Cu(beto)_2]^{2+/1+}$, and $[Cu(beto_{2Ox})_2]^{2+/1+}$ electrolytes (a) Photocurrent density vs voltage data measured for solar cells sensitized with Y123 dye under standard AM 1.5G illumination and in the dark (b) IPCE spectra of the liquid state DSC devices sensitized with Y123 dye.

Table 3. $J-V$ characteristics for the liquid state devices employing $[Cu(tmby)_2]^{2+/1+}$, $[Cu(beto)_2]^{2+/1+}$ and $[Cu(beto_{2Ox})_2]^{2+/1+}$ complexes under standard AM 1.5G illumination

Redox couple	V_{oc} (V)	J_{sc} (mA cm^{-2})	FF	PCE (%)
$[Cu(tmby)_2]^{2+/1+}$	1.087	11.815	0.786	10.06
$[Cu(beto)_2]^{2+/1+}$	1.08	12.392	0.781	10.42
$[Cu(beto_{2Ox})_2]^{2+/1+}$	1.01	11.851	0.783	10.18

complex $[Cu(beto)_2]^{2+/1+}$ compensates for this, resulting in a very similar V_{oc} for these complexes. The slightly higher short-circuit current density obtained with the $[Cu(beto)_2]^{2+/1+}$ electrolyte is attributed to the slightly higher driving force available for dye regeneration and less parasitic absorption of the electrolyte due to lower solubility of Cu(I) species, confirmed by higher incident photon-to-current conversion efficiency (IPCE). The FF values stayed similar in liquid state DSCs with all the complexes.

The IPCE spectra for the liquid state devices employing $[Cu(beto)_2]^{2+/1+}$, $[Cu(beto_{2Ox})_2]^{2+/1+}$, and $[Cu(tmby)_2]^{2+/1+}$ are given in Figure 6b. For the $[Cu(beto)_2]^{2+/1+}$ electrolyte, the maximum IPCE is found at 400 nm as 80%. For $[Cu(beto_{2Ox})_2]^{2+/1+}$ and $[Cu(tmby)_2]^{2+/1+}$ electrolytes, the IPCE maxima stayed around 70%. The lower IPCE values for $[Cu(beto_{2Ox})_2]^{2+/1+}$ and $[Cu(tmby)_2]^{2+/1+}$ are attributed to the slightly higher parasitic absorptions of these electrolytes in comparison to that of $[Cu(beto)_2]^{2+/1+}$, which has fewer copper species in the electrolyte (due to poor solubility) and therefore induces less parasitic absorption.

For the introduced new copper complexes, which exhibit poorer photovoltaic performance in the solid compared to the liquid state, typical JV data of the zombie devices prepared by Y123 sensitized TiO$_2$ films that employ solid copper complex HTMs are given in Figure 7. The J_{sc}, V_{oc}, FF, and PCE of these devices are also given in Table 4. Contrary to the $[Cu(tmby)_2]^{2+/1+}$ HTM,[37] $[Cu(beto)_2]^{2+/1+}$ and $[Cu(beto_{2Ox})_2]^{2+/1+}$ HTMs exhibit hysteresis in reverse and forward voltage scans (Figure S4). In order to obtain the acceptably shaped IV curves, the devices employing $[Cu-$
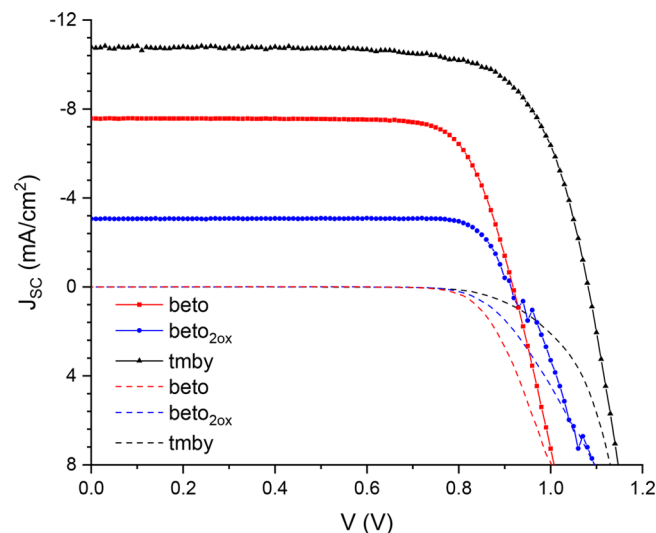

Figure 7. Current density−voltage ($J-V$) characteristics of Y123 sensitized zombie devices employing $[Cu(beto)_2]^{2+/1+}$, $[Cu(beto_{2Ox})_2]^{2+/1+}$, and $[Cu(tmby)_2]^{2+/1+}$ complexes under standard AM 1.5G illumination and in the dark (the scan settling time is 0.08 s for $[Cu(beto_{2Ox})_2]^{2+/1+}$ and 0.04 s for $[Cu(beto)_2]^{2+/1+}$ and $[Cu(tmby)_2]^{2+/1+}$, respectively).

Table 4. $J-V$ Characteristics for the Typical Zombie Devices Employing $[Cu(beto)_2]^{2+/1+}$, $[Cu(beto_{2Ox})_2]^{2+/1+}$, and $[Cu(tmby)_2]^{2+/1+}$ Complexes under Standard AM 1.5G Illumination^a

Redox couple	V_{oc} (V)	J_{sc} (mA cm^{-2})	FF	PCE (%)
$[Cu(tmby)_2]^{2+/1+}$	1.082	10.79	0.727	8.48
$[Cu(beto)_2]^{2+/1+}$	0.918	7.57	0.772	5.43
$[Cu(beto_{2Ox})_2]^{2+/1+}$	0.911	3.06	0.841	2.36

^{a}The scan settling time is 0.08 s for $[Cu(beto_{2Ox})_2]^{2+/1+}$ and 0.04 s for $[Cu(beto)_2]^{2+/1+}$ and $[Cu(tmby)_2]^{2+/1+}$, respectively.

$[Cu(beto_{2Ox})_2]^{2+/1+}$ need slower voltage scan settling times. For $[Cu(beto)_2]^{2+/1+}$ and $[Cu(tmby)_2]^{2+/1+}$, the IV scan settling time is 0.04 s, whereas for $[Cu(beto_{2Ox})_2]^{2+/1+}$, it is 0.08 s.
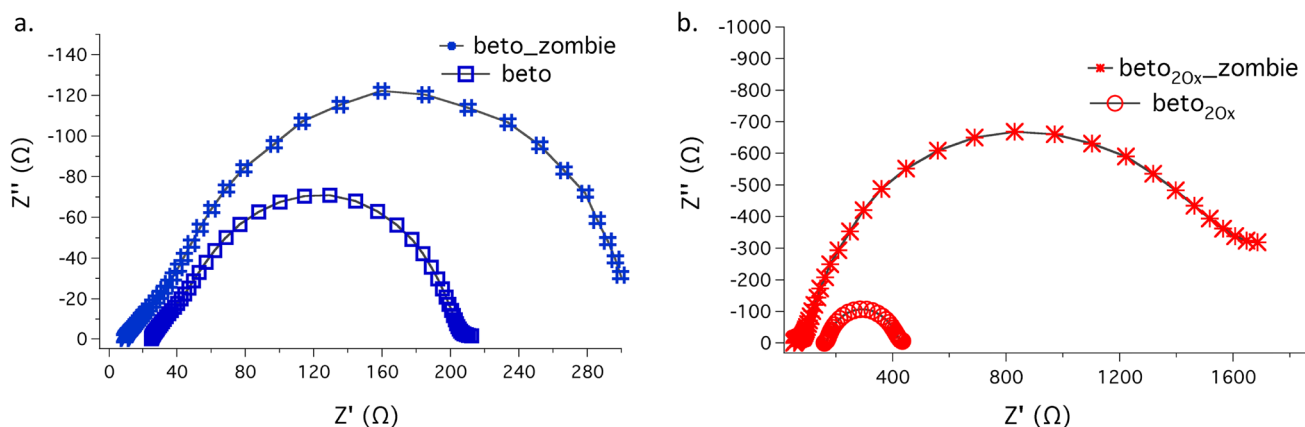
Figure 8. Nyquist plots of the dark electrochemical impedance spectra measured at an applied potential bias of −900 mV for liquid state and solid state devices employing (a) $[Cu(beto)_2]^{2+/1+}$ and (b) $[Cu(beto_{2Ox})_2]^{2+/1+}$complexes. In order to avoid crossing of the curves, the impedance spectra offsets are applied on the bottom axis as follows: $[Cu(beto)_2]^{2+/1+}$liquid state (18 Ωcm^2), $[Cu(beto_{2Ox})_2]^{2+/1+}$ liquid state (50 Ωcm^2).

According to Sarker et al.,[52] the hysteresis at open circuit potential originates due to the chemical capacitance at the counter electrode/electrolyte interface. This supports our experimental observation; therefore, we can state that $[Cu(beto_{2Ox})_2]^{2+/1+}$ and $[Cu(beto)_2]^{2+/1+}$ produce poorer electrical contact with the PEDOT counter electrode. The reasons for the poor photovoltaic performance of the solid-state devices are further investigated in terms of impedance spectroscopy and conductivity measurements as described below.

Electrochemical Impedance Spectroscopy. Electrochemical Impedance Spectroscopy (EIS) is used to investigate the effect of the copper redox mediators on liquid state devices, solid state devices, and symmetrical dummy cells. The liquid state devices, solid state devices, and dummy cells are represented by different equivalent circuits due to charge transport and cell component differences (see Figure S5). Fittings based on these equivalent circuits provide the following parameters: R_{series} is the ohmic serial resistance; R_{CE} is the charge-transfer resistance at the counter electrode; CPce (constant phase element) is used to account for the roughness of the PEDOT counter electrode.[53−55] R_{CT} is the recombination resistance, and CPEu is the corresponding phase element.

The impedance of the constant phase element (CPce and CPEu) ($0\leq \beta \leq 1$) equals

$$Z_{CPE} = B^{-1} \cdot (i\omega)^{-\beta} \qquad (3)$$

where ω is the frequency, B and β are the frequency-independent parameters of the CPE; the corresponding parameters are 'CPE-T' = B and 'CPE-P' = β. For liquid state devices, the low-frequency part of the spectrum is dominated by the Warburg impedance and it can be modeled by a finite-length element W_s with the parameters 'W_s-R' =R_W, 'W_s-T' = T_W, and 'Ws-P' = 0.5.[56,57] The finite length Warburg diffusion impedance is then expressed as

$$Z_W = \frac{R_W}{\sqrt{iT_W\omega}}\tan h\sqrt{iT_W\omega} ; \qquad T_W = \frac{\delta^2}{D} \qquad (4)$$

For solid state devices, the hole transport is represented by a resistance (R1) coupled with a capacitance (CPE1) instead of the Warburg element.[37]

The Nyquist plots of the dark electrochemical impedance spectra and fitting parameters are provided in Figure 8 and Table S1, respectively (at −900 mV applied potential bias). For solid state devices, the increased R_{series} values imply that the solidified electrolyte has detrimental effects across the TCO/HTM and PEDOT/HTM interfaces, especially for the $[Cu(beto_{2Ox})_2]^{2+/1+}$zombie device (by assuming same transport resistance of the transparent conductive oxide (TCO)). For $[Cu(beto_{2Ox})_2]^{2+/1+}$, the R_{CE} value at the counter electrode rises due to poor PEDOT/HTM interface (Table S1). As observed in Figure 7, the liquid state devices and solid-state devices show profound differences especially in the Warburg related low frequency regions. For $[Cu(beto)_2]^{2+/1+}$, the Warburg resistance and hole transport resistances are obtained as 96 and 287 Ω for liquid and solid-state devices, respectively. For $[Cu(beto_{2Ox})_2]^{2+/1+}$, the Warburg resistance (70 Ω) and hole transport resistances (1541 Ω) show a greater variation, indicating much poorer charge transport for the solidified $[Cu(beto_{2Ox})_2]^{2+/1+}$ electrolyte.

In order to measure diffusion coefficients for the liquid electrolytes, symmetrical dummy cells were fabricated and analyzed by EIS. The Nyquist plots of EIS measured at 0 V are given in Figure S6. The diffusion coefficients can be calculated as 5.33 × 10^{-5}, 6.39 × 10^{-5}, and 4.37 × 10^{-5} for $[Cu(tmby)_2]^{2+/1+}$, $[Cu(beto)_2]^{2+/1+}$, and $[Cu(beto_{2Ox})_2]^{2+/1+}$, respectively, by using eq 4. (For the $[Cu(tmby)_2]^{2+/1+}$ electrolyte, the diffusion coefficient was reported as 2.6 × 10^{-5} cm^2/s, previously, for a similar system.[44]) The diffusion coefficient values can be analyzed with regard to the Dahms-Ruff mechanism (eq 5),[58,59] where the observed diffusion coefficient can be comprised of the mass transport by physical displacement of molecules (D_{mass}) and the electron-hopping contribution

$$D = D_{mass} + \frac{k_{ex}c\delta_{cc}^2}{6} \qquad (5)$$

where k_{ex} is electron self-exchange rate constant, and δ_{cc} is the center-to center distance. As reported earlier,[53] the contribution of the electron-hopping is negligible (10^{-13} cm^2/s) for similar Cu-complex liquid electrolytes. Therefore, higher diffusion coefficient values for $[Cu(tmby)_2]^{2+/1+}$ and $[Cu(beto)_2]^{2+/1+}$ are attributed to the smaller sizes of these complexes in comparison to the bulkier $[Cu(beto_{2Ox})_2]^{2+/1+}$.[28] For zombie devices, the hole transport process is presumed to

be determined by the hopping charge transfer process[53] since physical displacement of molecules is not expected and the δ_{cc} values increase with the aggregation of copper complexes. For $[Cu(beto)_2]^{2+/1+}$, we can assume a higher electron self-exchange rate constant in comparison to the bulkier $[Cu(beto_{2Ox})_2]^{2+/1+}$ and accordingly better hole transport (which is consistent with the lower HTM resistance value obtained from EIS). The conductivities of the HTMs were measured by interdigitated gold arrays. As observed in Figure 9, the $[Cu(beto)_2]^{2+/1+}$ and $[Cu(tmby)_2]^{2+/1+}$ showed better conductivities in comparison to that of $[Cu(beto_{2Ox})_2]^{2+/1+}$.
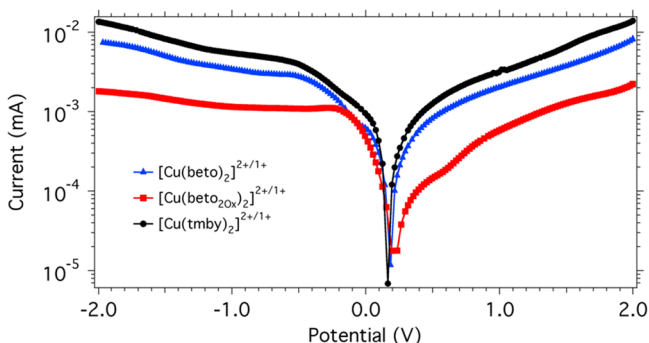
Figure 9. Current Voltage characteristics of HTM films on interdigitated Au electrodes (the HTMs deposited by drop-casting).

The poor charge transport with $[Cu(beto)_2]^{2+/1+}$ and $[Cu(beto_{2Ox})_2]^{2+/1+}$ can explain the obtained lower photovoltaic performance of these solid state devices. A poor electrical contact between the zombie HTM and PEDOT is another possibility. Interestingly, the diminished charge transport properties with $[Cu(beto)_2]^{2+/1}$ and $[Cu(beto_{2Ox})_2]^{2+/1+}$ only affects the J_{SC} values (Table 3). With low J_{SC} values, the obtained fill factor values are still high. The origin of this unusual result will be investigated in future studies.

CONCLUSION

We reported the synthesis, characterizations, and photovoltaic performances of two new copper redox mediators for dye-sensitized solar cells. The copper coordination complexes were obtained from 6,6′-dimethyl-2,2′-bipyridine ligands that were functionalized at the 4,4′ positions by ethoxy or methoxy−ethoxy chains. The resulting organometallic Cu(I) coordination complexes of these ligands showed reversible formal potentials of approximately 0.8 V vs SHE, which is negatively shifted by approximately 70 mV vs SHE compared to the standard $[Cu(tmby)_2]^{2+/+}$ redox couple. Single crystal X-ray diffraction measurements performed on $[Cu(beto)_2][TFSI]$ showed strong geometric similarities in the coordination sphere with $[Cu(tmby)_2]^+$, indicating that these new ligands did not affect the structural environment of the copper metal center. X-ray diffraction measurements showed that $[Cu(beto_{2Ox})_2]^{2+/1+}$ films had a reduced crystallinity compared to those of the films made of $[Cu(beto)_2]^{2+/1+}$ and $[Cu(tmby)_2]^{2+/1}$. Transient absorption spectroscopy showed that $[Cu(beto)_2]^{2+/1}$ and $[Cu(beto_{2Ox})_2]^{2+/1+}$ benefit from the higher driving force for dye regeneration, which allows them to have high dye regeneration efficiencies despite their bulkier structures. The performances of liquid DSCs fabricated with the new coordination complexes were found to be 10.4% and

10.2% for $[Cu(beto)_2]^{2+/1}$ and $[Cu(beto_{2Ox})_2]^{2+/1+}$ electrolytes, respectively, under AM 1.5G illumination. However, the zombie devices performed poorly in addition to presenting strong hysteresis. These findings were explained by the increased charge transfer resistances induced by the $[Cu(beto)_2]^{2+/1}$ and $[Cu(beto_{2Ox})_2]^{2+/1+}$ complexes as evidenced by electrochemical impedance spectroscopy and poorer PEDOT/HTM contact. We showed that structural modifications of the ligands based on a 6,6′-dimethyl-2,2′-bipyridine scaffold do not alter the photovoltaic performances of the liquid devices but change the morphology and charge transfer properties of the films in the zombie cells and photovoltaic performance accordingly.

ASSOCIATED CONTENT

Supporting Information

The Supporting Information is available free of charge at https://pubs.acs.org/doi/10.1021/acs.jpcc.0c00671.

Synthesis and characterization of the ligands and copper complexes, UV−vis spectra, XRD data, hysteresis and EIS data (PDF)

AUTHOR INFORMATION

Corresponding Author

Anders Hagfeldt − *Laboratory of Photomolecular Science, Institute of Chemical Sciences and Engineering, École Polytechnique Fédérale de Lausanne, 1015 Lausanne, Switzerland;* orcid.org/0000-0001-6725-8856; Email: anders.hagfeldt@epfl.ch

Authors

Yasemin Saygili − *Laboratory of Photomolecular Science, Institute of Chemical Sciences and Engineering, École Polytechnique Fédérale de Lausanne, 1015 Lausanne, Switzerland*

Marko Stojanovic − *Laboratory for Photonics and Interfaces, Institute of Chemical Sciences, Engineering, École Polytechnique Fédérale de Lausanne, 1015 Lausanne, Switzerland*

Hui-Seon Kim − *Laboratory of Photomolecular Science, Institute of Chemical Sciences and Engineering, École Polytechnique Fédérale de Lausanne, 1015 Lausanne, Switzerland;* orcid.org/0000-0002-9928-3033

Joel Teuscher − *Photochemical Dynamics Group, Ecole Polytechnique Fédérale de Lausanne, 1015 Lausanne, Switzerland*

Rosario Scopelliti − *Institut des Sciences et Ingenierie Chimiques, Ecole Polytechnique Fédérale de Lausanne, 1015 Lausanne, Switzerland;* orcid.org/0000-0001-8161-8715

Marina Freitag − *Department of Chemistry- Ångström Laboratory, Uppsala University, 751 20 Uppsala, Sweden;* orcid.org/0000-0002-4954-6851

Shaik M. Zakeeruddin − *Laboratory of Photomolecular Science, Institute of Chemical Sciences and Engineering, École Polytechnique Fédérale de Lausanne, 1015 Lausanne, Switzerland*

Jacques-E. Moser − *Photochemical Dynamics Group, Ecole Polytechnique Fédérale de Lausanne, 1015 Lausanne, Switzerland;* orcid.org/0000-0003-0747-4666

Michael Grätzel − *Laboratory for Photonics and Interfaces, Institute of Chemical Sciences, Engineering, École Polytechnique Fédérale de Lausanne, 1015 Lausanne, Switzerland;* orcid.org/0000-0002-0068-0195

■ REFERENCES

(1) Yun, S.; Qin, Y.; Uhl, A. R.; Vlachopoulos, N.; Yin, M.; Li, D. D.; Han, X.; Hagfeldt, A. New-Generation Integrated Devices Based on Dye-Sensitized and Perovskite Solar Cells. *Energy Environ. Sci.* **2018**, *476*, 476−526.

(2) Grätzel, M. Dye-Sensitized Solar Cells. *J. Photochem. Photobiol., C* **2003**, *4*, 145−153.

(3) Mozaffari, S.; Nateghi, M. R.; Zarandi, M. B. An Overview of the Challenges in the Commercialization of Dye Sensitized Solar Cells. *Renewable Sustainable Energy Rev.* **2017**, *71*, 675−686.

(4) Sharma, S.; Bulkesh, Siwach; Ghoshal, S. K.; Mohan, D. Dye Sensitized Solar Cells: From Genesis to Recent Drifts. *Renewable Sustainable Energy Rev.* **2017**, *70*, 529−537.

(5) Allardyce, C. S.; Fankhauser, C.; Zakeeruddin, S. M.; Grätzel, M.; Dyson, P. J. The Influence of Greenhouse-Integrated Photovoltaics on Crop Production. *Sol. Energy* **2017**, *155*, 517−522.

(6) Sun, J.; Jasieniak, J. J. Semi-Transparent Solar Cells. *J. Phys. D: Appl. Phys.* **2017**, *50*, 9.

(7) Cao, Y.; Liu, Y.; Zakeeruddin, S. M.; Hagfeldt, A.; Grätzel, M. Direct Contact of Selective Charge Extraction Layers Enables High-Efficiency Molecular Photovoltaics. *Joule* **2018**, *2*, 1108−1117.

(8) Freitag, M.; Teuscher, J.; Saygili, Y.; Zhang, X.; Giordano, F.; Liska, P.; Hua, J.; Zakeeruddin, S. M.; Moser, J.-E.; Grätzel, M.; et al. Dye-Sensitized Solar Cells for Efficient Power Generation under Ambient Lighting. *Nat. Photonics* **2017**, *11*, 372−378.

(9) O'Regan, B.; Gratzel, M. A Low-Cost, High-Efficiency Solar Cell Based on Dye-Sensitized Colloidal TiO2 Films. *Nature* **1991**, *353*, 737−740.

(10) Yao, Z.; Zhang, M.; Li, R.; Yang, L.; Qiao, Y.; Wang, P. A Metal-Free n-Annulated Thienocyclopentaperylene Dye: Power Conversion Efficiency of 12% for Dye-Sensitized Solar Cells. *Angew. Chem., Int. Ed.* **2015**, *54*, 5994−5998.

(11) Hagberg, D. P.; Jiang, X.; Gabrielsson, E.; Linder, M.; Marinado, T.; Brinck, T.; Hagfeldt, A.; Sun, L. Symmetric and Unsymmetric Donor Functionalization. Comparing Structural and Spectral Benefits of Chromophores for Dye-Sensitized Solar Cells. *J. Mater. Chem.* **2009**, *19*, 7232−7238.

(12) Yum, J.; Holcombe, T. W.; Kim, Y.; Rakstys, K.; Moehl, T.; Teuscher, J.; Delcamp, J. H.; Nazeeruddin, M. K.; Grätzel, M. Blue-Coloured Highly Efficient Dye-Sensitized Solar Cells by Implementing the Diketopyrrolopyrrole Chromophore. *Sci. Rep.* **2013**, *3*, 2446.

(13) Ren, Y.; Sun, D.; Cao, Y.; Tsao, H. N.; Yuan, Y.; Zakeeruddin, S. M.; Wang, P.; Grätzel, M. A Stable Blue Photosensitizer for Color Palette of Dye-Sensitized Solar Cells Reaching 12.6% Efficiency. *J. Am. Chem. Soc.* **2018**, *140*, 2405−2408.

(14) Wu, Y.; Zhu, W. Organic Sensitizers from D−π−A to D−A−π−A: Effect of the Internal Electron-Withdrawing Units on Molecular Absorption, Energy Levels and Photovoltaic Performances. *Chem. Soc. Rev.* **2013**, *42*, 2039−2058.

(15) Bella, F.; Galliano, S.; Gerbaldi, C.; Viscardi, G. Cobalt-Based Electrolytes for Dye-Sensitized Solar Cells: Recent Advances towards Stable Devices. *Energies* **2016**, *9*, 384.

(16) Magni, M.; Biagini, P.; Colombo, A.; Dragonetti, C.; Roberto, D.; Valore, A. Versatile Copper Complexes as a Convenient Springboard for Both Dyes and Redox Mediators in Dye Sensitized Solar Cells. *Coord. Chem. Rev.* **2016**, *322*, 69−93.

(17) Hagfeldt, A.; Boschloo, G.; Sun, L.; Kloo, L.; Pettersson, H. Dye-Sensitized Solar Cells. *Chem. Rev.* **2010**, *110*, 6595−6663.

(18) Saygili, Y.; Stojanovic, M.; Flores-Díaz, N.; Zakeeruddin, S. M.; Vlachopoulos, N.; Grätzel, M.; Hagfeldt, A. Metal Coordination Complexes as Redox Mediators in Regenerative Dye-Sensitized Solar Cells. *Inorganics* **2019**, *7*, 30.

(19) Benesperi, I.; Michaels, H.; Freitag, M. The Researcher's Guide to Solid-State Dye-Sensitized Solar Cells. *J. Mater. Chem. C* **2018**, *6*, 11903−11942.

(20) Rorabacher, D. B. Electron Transfer by Copper Centers. *Chem. Rev.* **2004**, *104*, 651−698.

(21) Feldt, S. M.; Wang, G.; Boschloo, G.; Hagfeldt, A. Effects of Driving Forces for Recombination and Regeneration on the Photovoltaic Performance of Dye-Sensitized Solar Cells Using Cobalt Polypyridine Redox Couples. *J. Phys. Chem. C* **2011**, *115*, 21500−21507.

(22) Yella, a.; Lee, H.-W.; Tsao, H. N.; Yi, C.; Chandiran, a. K.; Nazeeruddin, M. K.; Diau, E. W.-G.; Yeh, C.-Y.; Zakeeruddin, S. M.; Gratzel, M. Porphyrin-Sensitized Solar Cells with Cobalt (II/III)-Based Redox Electrolyte Exceed 12% Efficiency. *Science* **2011**, *334*, 629−634.

(23) Mathew, S.; Yella, A.; Gao, P.; Humphry-Baker, R.; Curchod, B. F. E.; Ashari-Astani, N.; Tavernelli, I.; Rothlisberger, U.; Nazeeruddin, M.. K.; Gratzel, M. Dye-sensitized solar cells with 13% efficiency achieved through the molecular engineering of porphyrin sensitizers. *Nat. Chem.* **2014**, *6*, 242−247.

(24) Feldt, S. M.; Lohse, P. W.; Kessler, F.; Nazeeruddin, M. K.; Gratzel, M.; Boschloo, G.; Hagfeldt, A. Regeneration and Recombination Kinetics in Cobalt Polypyridine Based Dye-Sensitized Solar Cells, Explained Using Marcus Theory. *Phys. Chem. Chem. Phys.* **2013**, *15*, 7087−7097.

(25) Saygili, Y.; Söderberg, M.; Pellet, N.; Giordano, F.; Cao, Y.; Muñoz-García, A. B.; Zakeeruddin, S. M. S. M.; Vlachopoulos, N.; Pavone, M.; Boschloo, G.; et al. Copper Bipyridyl Redox Mediators for Dye-Sensitized Solar Cells with High Photovoltage. *J. Am. Chem. Soc.* **2016**, *138*, 15087−15096.

(26) Liu, Z.; Duan, K.; Guo, H.; Deng, Y.; Huang, H.; Yi, X.; Chen, H.; Tan, S. The Enhancement of Photovoltaic Properties of the DSSCs Based on D−A−π−A Organic Dyes via Tuning Auxiliary Acceptor. *Dyes Pigm.* **2017**, *140*, 312−319.

(27) Feldt, S. M.; Gibson, E. A.; Gabrielsson, E.; Sun, L.; Boschloo, G.; Hagfeldt, A. Design of Organic Dyes and Cobalt Polypyridine Redox Mediators for High-Efficiency Dye-Sensitized Solar Cells. *J. Am. Chem. Soc.* **2010**, *132*, 16714−16724.

(28) Freitag, M.; Giordano, F.; Yang, W.; Pazoki, M.; Hao, Y.; Zietz, B.; Gra, M.; Hagfeldt, A.; Boschloo, G. Copper Phenanthroline as a Fast and High-Performance Redox Mediator for Dye-Sensitized Solar Cells. *J. Phys. Chem. C* **2016**, *120*, 9595−9603.

(29) Liang, M.; Chen, J. Arylamine Organic Dyes for Dye-Sensitized Solar Cells. *Chem. Soc. Rev.* **2013**, *42*, 3453−3488.

(30) O'Regan, B.; Lenzmann, F.; Muis, R.; Wienke, J. A Solid-State Dye-Sensitized Solar Cell Fabricated with Pressure-Treated P25−TiO2 and CuSCN: Analysis of Pore Filling and IV Characteristics. *Chem. Mater.* **2002**, *14*, 5023−5029.

(31) Tennakone, K.; Kumara, G. R. R. A.; Kottegoda, I. R. M.; Wijayantha, K. G. U.; Perera, V. P. S. A Solid-State Photovoltaic Cell Sensitized with a Ruthenium Bipyridyl Complex. *J. Phys. D: Appl. Phys.* **1998**, *31*, 1492.

(32) Zhang, J.; Vlachopoulos, N.; Jouini, M.; Johansson, M. B.; Zhang, X.; Nazeeruddin, M. K.; Boschloo, G.; Johansson, E. M. J.; Hagfeldt, A. Efficient Solid-State Dye Sensitized Solar Cells: The Influence of Dye Molecular Structures for the in-Situ Photo-

electrochemically Polymerized PEDOT as Hole Transporting Material. *Nano Energy* **2016**, *19*, 455−470.

(33) Xu, B.; Gabrielsson, E.; Safdari, M.; Cheng, M.; Hua, Y.; Tian, H.; Gardner, J. M.; Kloo, L.; Sun, L. 1,1,2,2-Tetrachloroethane (TeCA) as a Solvent Additive for Organic Hole Transport Materials and Its Application in Highly Efficient Solid-State Dye-Sensitized Solar Cells. *Adv. Energy Mater.* **2015**, *5*, 1402340.

(34) Lee, B.; Stoumpos, C. C.; Zhou, N.; Hao, F.; Malliakas, C.; Yeh, C.-Y.; Marks, T. J.; Kanatzidis, M. G.; Chang, R. P. H. Air-Stable Molecular Semiconducting Iodosalts for Solar Cell Applications: Cs2SnI6 as a Hole Conductor. *J. Am. Chem. Soc.* **2014**, *136*, 15379−15385.

(35) Freitag, M.; Daniel, Q.; Pazoki, M.; Sveinbjornsson, K.; Zhang, J.; Sun, L.; Hagfeldt, A.; Boschloo, G.; Sveinbjörnsson, K.; Zhang, J.; et al. High-Efficiency Dye-Sensitized Solar Cells with Molecular Copper Phenanthroline as Solid Hole Conductor. *Energy Environ. Sci.* **2015**, *8*, 2634−2637.

(36) Kashif, M. K.; Milhuisen, R. A.; Nippe, M.; Hellerstedt, J.; Zee, D. Z.; Duffy, N. W.; Halstead, B.; De Angelis, F.; Fantacci, S.; Fuhrer, M. S. Cobalt Polypyridyl Complexes as Transparent Solution-Processable Solid-State Charge Transport Materials. *Adv. Energy Mater.* **2016**, *6*, 1600874.

(37) Cao, Y.; Saygili, Y.; Ummadisingu, A.; Teuscher, J.; Luo, J.; Pellet, N.; Giordano, F.; Zakeeruddin, S. M. S. M.; Moser, J.-E. J.-E.; Freitag, M.; et al. 11% Efficiency Solid-State Dye-Sensitized Solar Cells with Copper(II/I) Hole Transport Materials. *Nat. Commun.* **2017**, *8*, 15390.

(38) Zhang, W.; Wu, Y.; Bahng, H. W.; Cao, Y.; Yi, C.; Saygili, Y.; Luo, J.; Liu, Y.; Kavan, L.; Moser, J. E.; et al. Comprehensive Control of Voltage Loss Enables 11.7% Efficient Solid-State Dye-Sensitized Solar Cells. *Energy Environ. Sci.* **2018**, *11*, 1779−1787.

(39) Ding, I.-K.; Tétreault, N.; Brillet, J.; Hardin, B. E.; Smith, E. H.; Rosenthal, S. J.; Sauvage, F.; Grätzel, M.; McGehee, M. D. Pore-Filling of Spiro-OMeTAD in Solid-State Dye Sensitized Solar Cells: Quantification, Mechanism, and Consequences for Device Performance. *Adv. Funct. Mater.* **2009**, *19*, 2431−2436.

(40) Malinauskas, T.; Tomkute-Luksiene, D.; Sens, R.; Daskeviciene, M.; Send, R.; Wonneberger, H.; Jankauskas, V.; Bruder, I.; Getautis, V. Enhancing Thermal Stability and Lifetime of Solid-State Dye-Sensitized Solar Cells via Molecular Engineering of the Hole-Transporting Material Spiro-OMeTAD. *ACS Appl. Mater. Interfaces* **2015**, *7*, 11107−11116.

(41) Kovalevsky, A. Y.; Gembicky, M.; Novozhilova, I. V.; Coppens, P. Solid-State Structure Dependence of the Molecular Distortion and Spectroscopic Properties of the Cu(I) Bis(2,9-Dimethyl-1,10-Phenanthroline) Ion. *Inorg. Chem.* **2003**, *42*, 8794−8802.

(42) Housecroft, C. E.; Constable, E. C. The Emergence of Copper(I)-Based Dye Sensitized Solar Cells. *Chem. Soc. Rev.* **2015**, *44*, 8386−8398.

(43) Haanstra, W. G.; Driessen, W. L.; Reedijk, J.; Cabral, M. F.; de Cabral, J. O. Unusually High Redox Potentials of Two Copper(II) Compounds of 1,8-Bis(3,5-Dimethyl-1-Pyrazolyl)-3,6-Dithiaoctane. *Inorg. Chem.* **1992**, *31*, 3150−3151.

(44) Ferdowsi, P.; Saygili, Y.; Zakeeruddin, S. M.; Mokhtari, J.; Grätzel, M.; Hagfeldt, A.; Kavan, L. Alternative Bases to 4-Tert-Butylpyridine for Dye-Sensitized Solar Cells Employing Copper Redox Mediator. *Electrochim. Acta* **2018**, *265*, 194−201.

(45) Pavlishchuk, V. V.; Addison, A. W. Conversion Constants for Redox Potentials Measured versus Different Reference Electrodes in Acetonitrile Solutions at 25°C. *Inorg. Chim. Acta* **2000**, *298*, 97−102.

(46) Ellis, H.; Vlachopoulos, N.; Haggman, L.; Perruchot, C.; Jouini, M.; Boschloo, G.; Hagfeldt, A. PEDOT Counter Electrodes for Dye-Sensitized Solar Cells Prepared by Aqueous Micellar Electrodeposition. *Electrochim. Acta* **2013**, *107*, 45−51.

(47) Fabregat-Santiago, F.; Bisquert, J.; Garcia-Belmonte, G.; Boschloo, G.; Hagfeldt, A. Influence of Electrolyte in Transport and Recombination in Dye-Sensitized Solar Cells Studied by Impedance Spectroscopy. *Sol. Energy Mater. Sol. Cells* **2005**, *87*, 117−131.

(48) Zhang, X.; Xu, Y.; Giordano, F.; Schreier, M.; Pellet, N.; Hu, Y.; Yi, C.; Robertson, N.; Hua, J.; Zakeeruddin, S. M.; et al. Molecular Engineering of Potent Sensitizers for Very Efficient Light Harvesting in Thin-Film Solid-State Dye-Sensitized Solar Cells. *J. Am. Chem. Soc.* **2016**, *138*, 10742−10745.

(49) Burke, P. J.; Henrick, K.; McMillin, D. R. Crystal and Molecular Structures of Bis(4,4′,6,6′-Tetramethyl-2,2′-Bipyridyl)Copper(I) Perchlorate, Bis(4,4′,6,6′-Tetramethyl-2,2′-Bipyridyl)Copper(II) Diperchlorate, and Bis(4,4′,6,6′-Tetramethyl-2,2′-Bipyridyl)Copper(II) Diperchlorate Dihydrate. A Searc. *Inorg. Chem.* **1982**, *21*, 1881−1886.

(50) Burke, P. J.; McMillin, D. R.; Robinson, W. R. Crystal and Molecular Structure of Bis(6,6′-Dimethyl-2,2′-Bipyridyl)Copper(I) Tetrafluoroborate. *Inorg. Chem.* **1980**, *19*, 1211−1214.

(51) Saygili, Y.; Stojanovic, M.; Michaels, H.; Tiepelt, J.; Teuscher, J.; Massaro, A.; Pavone, M.; Giordano, F.; Zakeeruddin, S. M.; Boschloo, G.; et al. The Effect of Coordination Sphere Geometry of Copper Redox Mediators on Regeneration and Recombination Behavior in Dye-Sensitized Solar Cell Applications. *ACS Appl. Energy Mater.* **2018**, *1*, 4950−4962.

(52) Sarker, S.; Seo, H. W.; Jin, Y.-K.; Lee, K.-S.; Lee, M.; Kim, D. M. On the Hysteresis of Current Density-Voltage Curves of Dye-Sensitized Solar Cells. *Electrochim. Acta* **2015**, *182*, 493−499.

(53) Kavan, L.; Saygili, Y.; Freitag, M.; Zakeeruddin, S. M. S. M.; Hagfeldt, A.; Grätzel, M. Electrochemical Properties of Cu(II/I)-Based Redox Mediators for Dye-Sensitized Solar Cells. *Electrochim. Acta* **2017**, *227*, 194−202.

(54) Kavan, L.; Krysova, H.; Janda, P.; Tarabkova, H.; Saygili, Y.; Freitag, M.; Zakeeruddin, S. M.; Hagfeldt, A.; Grätzel, M. Novel Highly Active Pt/Graphene Catalyst for Cathodes of Cu(II/I)-Mediated Dye-Sensitized Solar Cells. *Electrochim. Acta* **2017**, *251*, 167−175.

(55) Kavan, L.; Yum, J.-H.; Grätzel, M. Graphene Nanoplatelets Outperforming Platinum as the Electrocatalyst in Co-Bipyridine-Mediated Dye-Sensitized Solar Cells. *Nano Lett.* **2011**, *11*, 5501−5506.

(56) Kim, J.-Y.; Kim, J. Y.; Lee, D.-K.; Kim, B.; Kim, H.; Ko, M. J. Importance of 4-Tert-Butylpyridine in Electrolyte for Dye-Sensitized Solar Cells Employing SnO2 Electrode. *J. Phys. Chem. C* **2012**, *116*, 22759−22766.

(57) Kang, S. H.; Kim, J.-Y.; Kim, H. S.; Koh, H.-D.; Lee, J.-S.; Sung, Y.-E. Influence of Light Scattering Particles in the TiO2 Photoelectrode for Solid-State Dye-Sensitized Solar Cell. *J. Photochem. Photobiol., A* **2008**, *200*, 294−300.

(58) Blauch, D. N.; Saveant, J. M. Dynamics of Electron Hopping in Assemblies of Redox Centers. Percolation and Diffusion. *J. Am. Chem. Soc.* **1992**, *114*, 3323−3332.

(59) Barrosse-Antle, L. E.; Bond, A. M.; Compton, R. G.; O'Mahony, A. M.; Rogers, E. I.; Silvester, D. S. Voltammetry in Room Temperature Ionic Liquids: Comparisons and Contrasts with Conventional Electrochemical Solvents. *Chem. - Asian J.* **2010**, *5*, 202−230.

SUPPORTING INFORMATION

Liquid State and Zombie Dye Sensitized Solar Cells with Copper Bipyridine Complexes Functionalized with Alkoxy Groups

Yasemin Saygili[1+], Marko Stojanovic[2+], Hui-Seon Kim[1], Joel Teuscher[3], Rosario Scopelliti[5], Marina Freitag[4], Shaik M. Zakeeruddin[1], Jacques-E. Moser[3], Michael Grätzel[2], Anders Hagfeldt[1*]

[1]Laboratory of Photomolecular Science, Institute of Chemical Sciences and Engineering, École Polytechnique Fédérale de Lausanne , 1015, Lausanne, Switzerland.

[2]Laboratory for Photonics and Interfaces, Institute of Chemical Sciences, Engineering École Polytechnique Fédérale de Lausanne, 1015 Lausanne, Switzerland

[3]Photochemical Dynamics Group, Ecole Polytechnique Fédérale de Lausanne, 1015 Lausanne, Switzerland

[4] Department of Chemistry- Ångström Laboratory, Uppsala University, 751 20 Uppsala, Sweden

[5] Institut des Sciences et Ingenierie Chimiques, Ecole Polytechnique Fédérale de Lausanne, 1015 Lausanne, Switzerland

1. Synthesis of the Ligands

General information: Commercially available chemicals were used without any additional purification step. N,N-dimehtylformamide(DMF) was purchased over Molecular Sieve from ACROS Organics[TM], Sodium Hydride (NaH) was purchased as a moistened oil (55-65% wt) from Sigma Aldrich[TM]. ^{1}H and ^{13}C NMR spectra were recorded on Bruker AvanceIII-400 MHz NMR spectrometer. Chemical shifts are reported in parts per million (ppm, δ) and referenced to tetramethylsilane (0 ppm) or solvent residual peak (7.26 ppm for 1H NMR and 77.0 ppm for 13C NMR) as internal standard. Mass spectra were collected on a HITACHI-80 mass spectrometer.
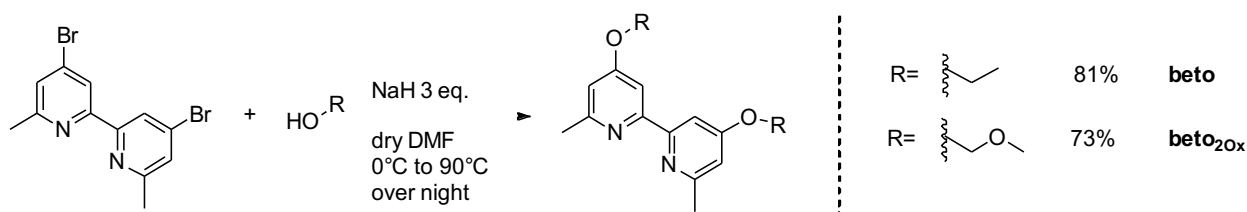
Scheme S1: Synthesis of beto and beto$_{2Ox}$ ligands.

4,4'-bis(2-methoxyethoxy)-6,6'-dimethyl-2,2'-bipyridine(**beto$_{2Ox}$**)
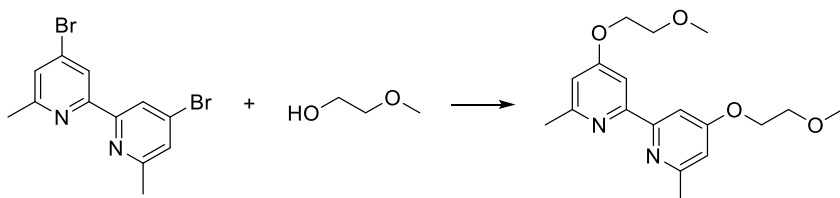
Sodium hydride (0.150 g, 6.14 mmol, 3 eq.) was added to 20 mL of anhydrous DMF at 0°C. The resulting suspension was stirred for 10 minutes after which 2-methoxyethan-1-ol (0.620 g, 8.19 mmol, 4 eq.) was added dropwise to afford the formation of hydrogen gas. The solution was then left at 0°C for 2 hours. 4,4'-dibromo-6,6'-dimethyl-2,2'-bipyridine (0.7 g, 2.05 mmol, 1 eq.) was added to the opaque mixture and the ice bath was removed to allow the reaction mixture to slowly warm up to room temperature. The beige opaque suspension was then heat at 90°C overnight. The dark green solution was then cooled down to RT, quenched with a saturated solution of ammonium chloride (200 mL). And the organics were extracted with DCM (3x100 mL). DCM was then removed and the residue dissolved in diethyl ether (100 mL). The organic phase was washed with deionized water (3x100 mL) and a saturated solution of sodium chloride (100 mL). The obtained yellow solution was dried over magnesium sulfate followed by evaporation of the diethyl ether. The product was obtained as a yellow solid 0.5 g (73% yield).

¹H NMR (400 MHz, Chloroform-d) δ 7.81 (d, J = 2.3 Hz, 2H), 6.75 (d, J = 2.3 Hz, 2H), 4.30 (t, J = 4.7 Hz, 5H), 3.81 (t, J = 4.7 Hz, 5H), 3.49 (s, 6H), 2.58 (s, 6H); ¹³C NMR (101 MHz, Chloroform-d) δ 166.03, 159.23, 157.56, 110.22, 104.32, 70.71, 67.07, 59.26, 24.71; MS (APPI⁺, m/z): [M+H⁺] calculated: 333.1809 found: 333.1809

4,4'-diethoxy-6,6'-dimethyl-2,2'-bipyridine(**beto**)
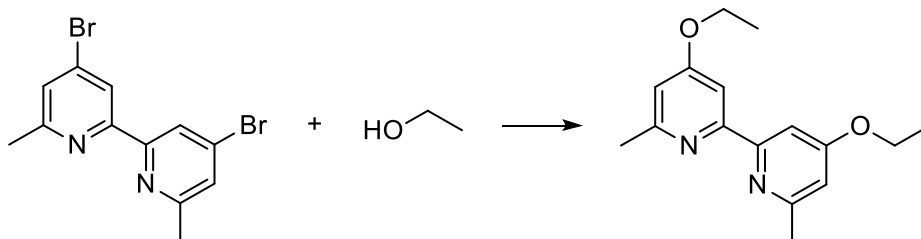
Sodium hydride (0.250 g, 10.53 mmol, 3 eq.) was added to 20 mL of anhydrous DMF at 0°C. The resulting suspension was stirred for 10 minutes after which 5 mL of Ethanol was added dropwise under vigorous stirring to afford the formation of hydrogen gas. The solution was then left at 0°C for 2 hours. 4,4'-dibromo-6,6'-dimethyl-2,2'-bipyridine (1.2 g, 3.51 mmol, 1 eq.) was added to the opaque mixture and the ice bath was removed to allow the reaction mixture to slowly warm up to room temperature. The beige opaque suspension was then heat at 65°C overnight. The dark green solution was then cooled down to RT, quenched with a saturated solution of ammonium chloride until neutral pH and diluted with deionized water. The organics were collected by extraction with Ether followed by drying over magnesium sulfate. The product was obtained as a beige crystalline solid: 0.671 g (70% yield).

¹H NMR (400 MHz, Chloroform-d) δ 7.76 (d, J = 2.3 Hz, 2H), 6.69 (d, J = 2.4 Hz, 2H), 4.21 (q, J = 7.0 Hz, 4H), 2.58 (s, 6H), 1.47 (t, J = 7.0 Hz, 6H); ¹³C NMR (101 MHz, Chloroform-d) δ 166.20, 159.16, 157.64, 109.89, 104.52, 63.44, 24.73, 14.63; MS (APPI⁺, m/z): [M+H⁺] calculated: 273.1598 found: 273.1600

2. Synthesis of the Cu(I) complexes

For [Cu(beto)₂][TFSI] and [Cu(beto₂Oₓ)₂][TFSI], one equivalent of CuI (35 mg, 0.175 mmol) was mixed with 3 equivalents of 4,4'-diethoxy-6.6'-dimethyl-2,2'-bipyridine (190mg, 0.7 mmol) or 4,4'-bis(2-methoxyethoxy)-6,6'-dimethyl-2,2'-bipyridine (232 mg, 0.7 mmol) in 20 ml ethanol, under nitrogen atmosphere, at room temperature for 2 hours. The resulted complex was obtained as intense orange/red, crystalline powder. The product was filtered and redissolved by addition of 5 ml of deionized water followed by an addition of 10 equivalents of LiTFSI (37 mg, 0.65 mmol). The solution was further stirred for 2 hours at room temperature and under nitrogen atmosphere resulting in orange/red precipitation. The
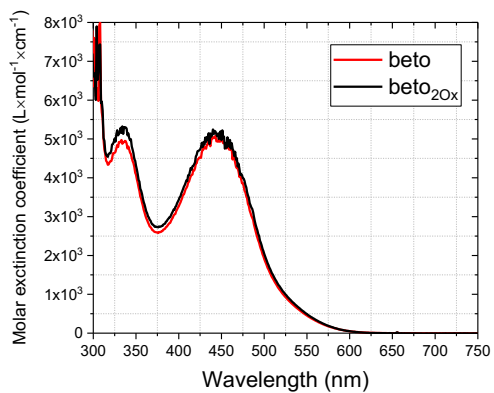
complex was collected by filtration and washed with water. The yield of the products over 80 % (mol).
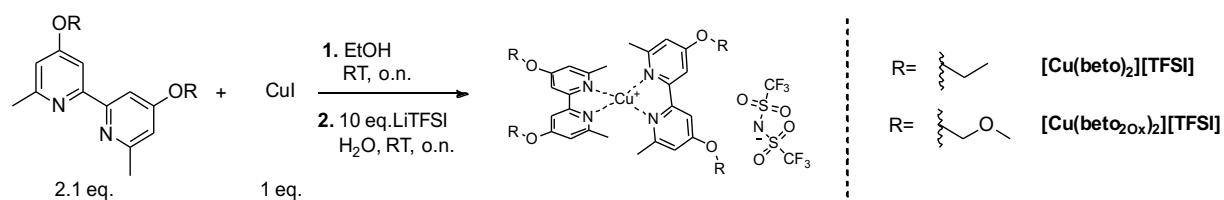
Scheme S2: Synthesis of [Cu(beto)₂][TFSI] and [Cu(beto₂Ox)₂][TFSI].

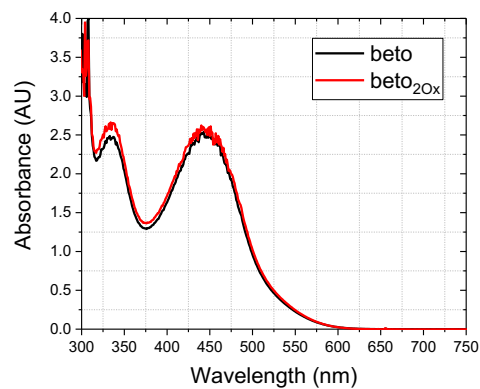## 3. UV-visible measurements.

a.

b.

Figure S1: a)Molar extinction coefficient of [Cu(beto)₂][TFSI](red) and [Cu(beto₂Ox)₂][TFSI](black). b) Absorption of [Cu(beto)₂][TFSI](red) and [Cu(beto₂Ox)₂][TFSI](black). Measured in 0.5 mM MeCN solution.
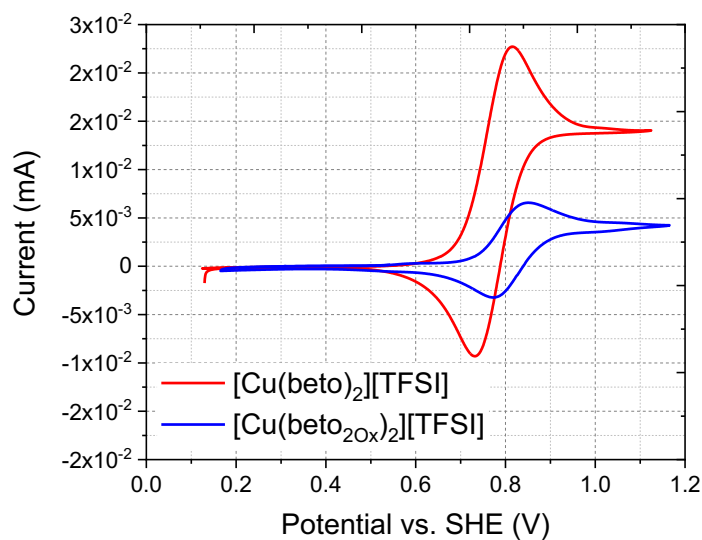
4. Electrochemical measurements

Figure S2:Cyclic voltamograms of [Cu(beto)₂][TFSI](red) and [Cu(beto₂ₒₓ)₂][TFSI](blue). (Measured in MeCN solution containing 0.1 M of LiTFSI as supporting electrolyte. The complexes concentrations were respectively 0.2 mM for [Cu(beto)₂][TFSI] and 0.5 mM for [Cu(beto₂ₒₓ)₂][TFSI]. The electrodes consisted in a Pt disk working electrode, a Pt wire counter electrode and a Ag/AgCl in saturated sodium chloride electrode.)
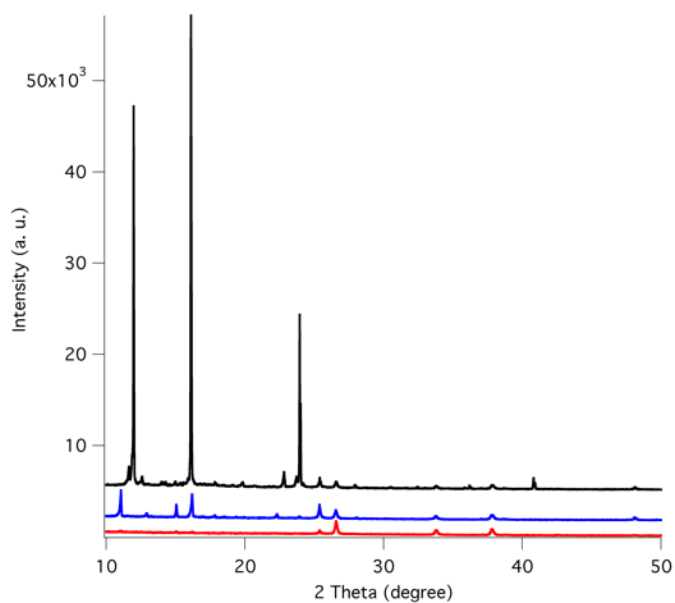
5. X-ray diffraction

Figure S3: XRD data of the dried [Cu(beto)₂]²⁺/¹⁺ (blue), [Cu(beto₂ₒₓ)₂]²⁺/¹⁺ (red), and [Cu(tmby)₂]²⁺/¹⁺ (black) electrolytes after drop-casting on top of a TiO₂ working electrode.

6. IV data
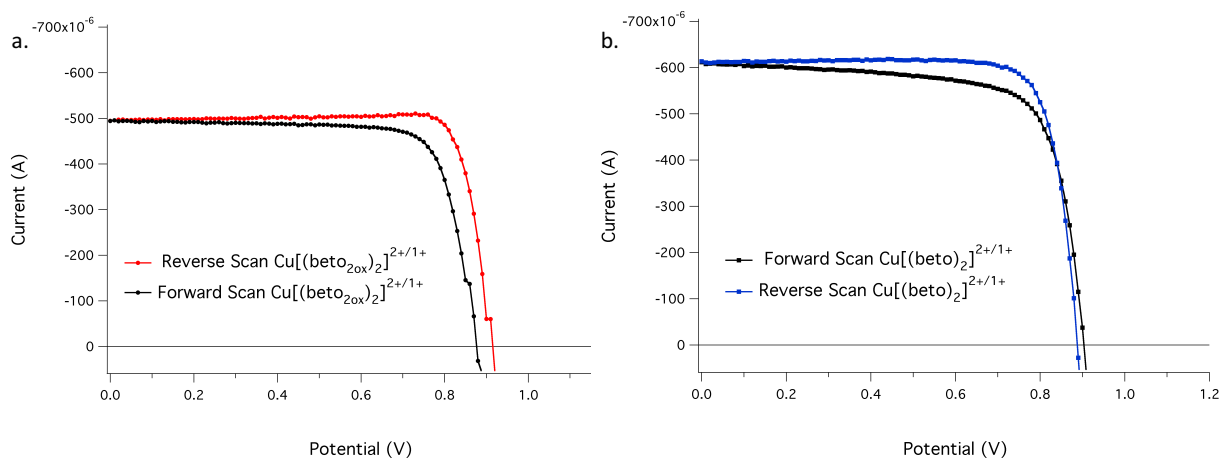
Figure S4: Hysteresis test for zombie devices employing a) [Cu(beto$_{2Ox}$)$_2$]$^{2+/1+}$ and b) [Cu(beto)$_2$]$^{2+/1+}$ complexes. (The scan settling time is 0.08 with 10mV/s voltage steps, the measurements are carried out with, 0.16 cm^2 mask).

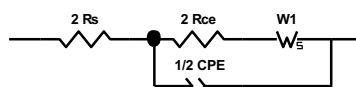## 7. Electrochemical Impedance Spectroscopy
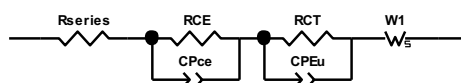
Figure S5: The equivalent circuits representing the liquid state devices, solid state devices and symmetrical dummy cells.

Table S1: Electrochemical parameters of the studied DSC devices with [Cu(beto)₂]²⁺/¹⁺ and [Cu(beto₂Ox)₂]²⁺/¹⁺ electrolytes.

|	$[Cu(beto)_2]^{2+/1+}$		$[Cu(beto_{2Ox})_2]^{2+/1+}$	
Device type	Liquid state	Zombie	Liquid state	Zombie
Rseries (Ω)	9.249	10.32	9.415	53.33
R_{CE} (Ω)	4.44	4.567	3.145	21.08
CPce-T	0.00010928	0.0000186	0.00003619	0.00032693
CPce-P	0.9	0.9	0.9	0.9
Rct (Ω)	79.26	30.59	181.6	32.51
CPEu-T	0.00027246	0.00011806	0.0001783	0.0000355
CPEu-P	0.84864	0.76275	0.96491	0.75102
W1-R (R1 for zombie)	95.99	287	69.6	1541
W1-T(CPEu-T for zombie)	0.022155	0.0000999	0.027274	0.0001082
W1_P(CPEu-P for zombie)	0.5	0.93188	0.5	0.91442
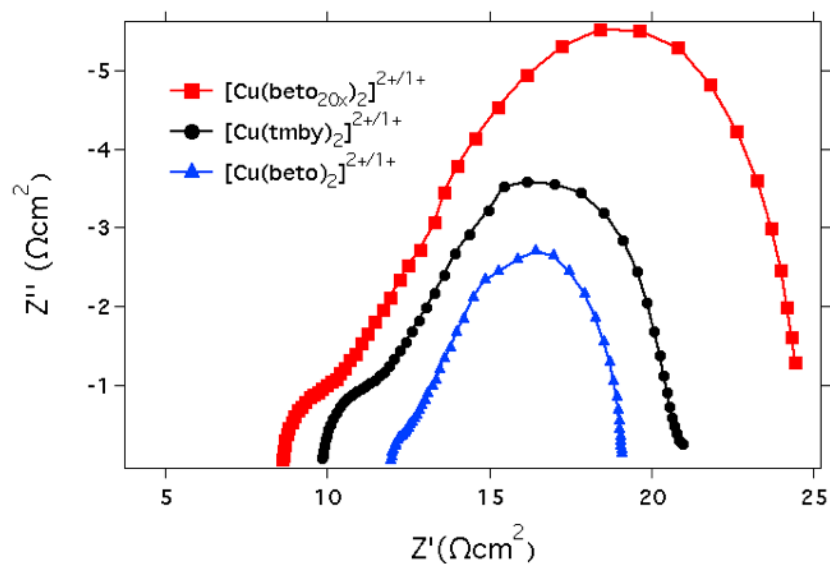
Figure S6: Nyquist plots of electrochemical impedance spectra measured at 0 V for the PEDOT/PEDOT symmetrical dummy cells. In order to avoid crossing of the curves, impedance spectra of the [Cu(beto)₂]²⁺/¹⁺ offset 4Ωcm² in the bottom axis.